BACHELOR

Investigation of a Packed-Bed Thermal Storage System for Industrial Application

Meerburg, Marten I.

Award date:
2023

Investigation of a Packed-Bed Thermal Storage System for Industrial Application

Author:
M.I. Meerburg
1598252

Supervisor:
C.C.M Rindt

Eindhoven University of Technology
Department of Mechanical Engineering
Energy Technology Group
Netherlands
July 7, 2023

Abstract

This study aims to investigate the effectiveness of a packed-bed thermal storage system for capturing waste heat generated during the sinter process in the steel industry. The specific temperature range of interest is 100-500°C. The main objectives of this research are to assess the system's performance using different heat transfer fluids and packing material sizes and to determine the required storage volume and mass flow rates. Additionally, the study includes an analysis of pressure drop during charging and discharging cycles, and the development of a numerical model to gain insights into the thermocline behavior. The different fluids and particle sizes showed to have a major influence on flow velocity and the heat transfer characteristics. Typical storage volumes were found to range from 1300-2000 m^3. For a minimal surface area storage tank the required mass flow rates were found to be 72 kg/s for air and salt, and 34 kg/s for oil. Pressure drop is only significant for air flow and increases strongly with particle diameters below ten centimeters. Lastly a numerical simulation is presented discussing the influence of various parameters on the thermocline behaviour.

Contents

Nomenclature

T	Temperature (°C)
Q	Energy (J)
q	Power (W)
p	Pressure (Pa)
d	Particle Diameter (m)
r	Particle Radius (m)
D	Tank Diameter (m)
L	Length (m)
V	Volume (m^3)
A	Area (m^2)
v	Velocity (m/s)
t	Time (s)
k	Conductivity (W/m °C)
h	Convective Heat Transfer Coefficient (W/m^2 °C)
c_p	Specific Heat Capacity (J/kg °C)
ρ	Density (kg/m^3)
μ	Viscosity (kg/m s)
α	Diffusivity (m^2/s)
ϵ	Porosity
ψ	Sphericity
Re	Reynolds Number
Nu	Nusselt Number
Bi	Biot Number
Fo	Fourier Number
θ	Dimensionless Temperature

Subscripts

s	Solid
f	Fluid
w	Wall
p	Particle
sf	Superficial
c	Characteristic
r	At particle surface
0	At particle core
$area$	Storage tank area
ext	Exterior
min	Minimum
max	Maximum
tot	Total

1. Introduction

To restrict global warming to 1.5 degrees Celsius, it is vital to attain net zero carbon emissions by 2050 as laid out in the Paris Agreement (Fletcher and Smith, 2020). Given that the industrial sector constitutes 25.6% of the global energy consumption (Eurostat, 2020), it is crucial to prioritize the decarbonization of the industrial energy system. The increasing environmental concern and growing demand for energy have prompted the industrial sector to reassess their energy utilization and recycling practices. Given that heat constitutes 47% of the energy consumption in the industrial sector (IEA, 2021), it is imperative to prioritize the efficient utilization of waste heat.

Packed-bed thermal storage (PBTS) systems are emerging as a promising solution for the recovery of industrial waste heat. PBTS systems work by circulating a heat transfer fluid (HTF) through a bed of solid particles, such as stone spheres, to store heat during times of excess energy production and release it in time of need. An illustration of such a PBTS system can be seen in Figure 1. The charging process of the PBTS system involves the injection of a high-temperature heat transfer fluid through the upper inlet of the tank, leading to the formation of a distinct thermocline region that effectively separates the hot and cold zones within the system. The thermocline is characterized by a sharp temperature gradient, with the upper layer at a higher temperature than the lower layer, which helps maintain the thermal stratification necessary for efficient energy storage. During the discharge phase, the stored heat is extracted by circulating a colder fluid through the lower outlet of the tank, facilitating the retrieval of the thermal energy.

These systems are an attractive option for the storage of waste heat due to several key factors. Firstly, they offer a comparatively lower capacity cost than other conventional energy storage devices. The cost of energy storage in a PBTS system is estimated to be €34/kWh, while the cost for storing energy in a lithium-ion battery is estimated to be €600/kWh (Strasser and Selvam, 2012). Secondly this system is known for its simplicity, high reliability and low maintenance. Lastly, these systems have significant potential for large-scale application, further adding to their attractiveness as a waste heat storage solution. Prior research has indicated that the widespread implementation of thermal energy storage in the EU's industrial sector have the potential to replace approximately 1793 TWh of fossil fuel consumption with surplus heat. This transition could lead to a significant reduction of 513 Mton CO_2 equivalent in annual green house gas emissions (Ulusoy, 2019).

Numerous test setups have been deployed to explore the recovery of waste heat using PBTS systems. These test setups aim to assess the performance, efficiency, and reliability of PBTS systems under various operating conditions. An example of one of these test setups is the RESlag project on a steel recycling plant in ArcelorMittal, Spain (Ortega-Fernández and Rodríguez-Aseguinolaza, 2019). A pilot system was

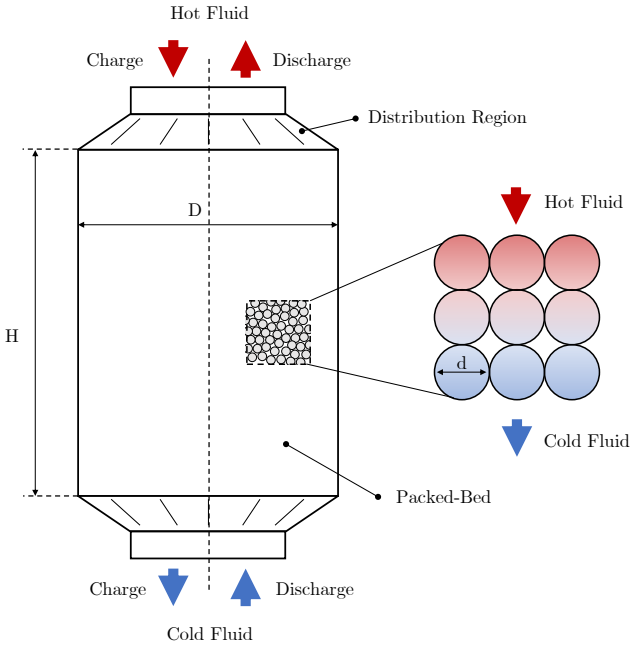

Figure 1: Schematic representation of packed bed storage system. The system comprises a storage tank with designated height and diameter dimensions denoted as H and D respectively. Within the tank, spherical rocks with diameter d are utilized as the medium for heat storage. The red colour indicates a high temperature region and the blue colour a lower temperature region.

build, featuring a storage volume of 3 m^3 and an energy capacity of 3.6 GJ, to utilize steel slag as a medium for storing residual heat from an electric arc furnace. The experimental findings demonstrated a reduction of approximately 4% in CO_2 emissions per ton of steel produced. SIEMENS Gamesa's Carnot battery pilot plant serves as a prominent illustration of a large-scale application. This pilot project employs a packed bed composed of Basalt and utilizes air as the heat transfer medium, enabling the storage of 470 GJ of heat with a heating power of 30 MW. The ambiguous objective of this project is to upscale the system's capacity to store multiple Terajoule, equivalent to the energy consumption of several hundred thousand households (Seyitini et al., 2023).

Figure 2: SIEMENS Gamesa's Carnot battery pilot plant located in Hamburg-Altenwerder (Gamesa, 2022)

During this study a cylindrical PBTS system will be considered with spherical rock material for heat storage. The PBTS unit will be examined for its compatibility with the process of sintering, an energy intensive batch process from the steel industry. The operational temperature range for the system will span from 100°C to 500°C. The performance analysis of the PBTS system, tailored to the sintering application, will encompass diverse aspects, including the evaluation of different HTFs and storage materials, examination of various sizes of packing material and determination of the required storage volume and HTF mass flows. The primary objective of this study is to investigate the influence of these aspects on the operational characteristics of the PBTS system.

Before describing the various technical aspects of the system an examination of the selected industrial process and its heat supplying characteristics is presented in chapter two. Subsequently, chapter three gives a comprehensive review regarding the diverse numerical models developed to assess cylindrical packed bed thermal storage systems. Chapter four proceeds by discussing some typical heat transfer fluids and solid storage media that can be utilized for the storage of thermal energy. Several key characteristics of the system are identified after which some typical storage volumes, tank dimensions and mass flows are provided. In chapter five insights are given into relevant dimensionless numbers that are useful for classifying the system. Chapter six evaluates the pressure loss incurred during the charging and discharging of the system. Finally, a simplified numerical model is presented in chapter seven, accompanied by a conclusion in chapter eight.

2. Industry Waste Heat

The industrial sector is known for its substantial demand for energy, fueled by manufacturing processes, production lines, and various other operations. This sector encompasses a wide range of industries, including chemicals, minerals, and metals. An overview of the waste heat potential in the European union can be seen in Figure 3.

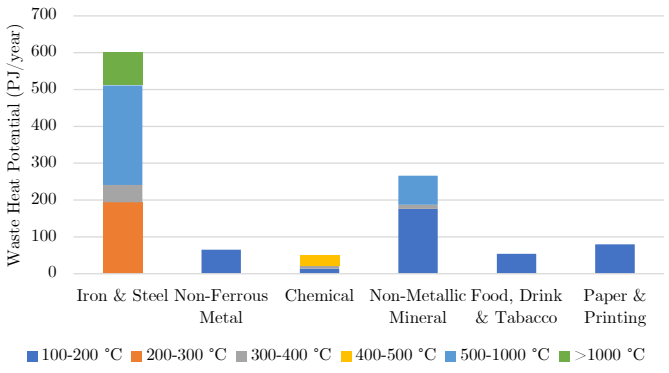

Figure 3: Overview of the total waste heat potential in Europe across different industrial sectors, along with corresponding temperature ranges associated with the waste heat. (Papapetrou et al., 2018)

The data reveals a significant waste heat potential within the temperature range of 100-200 °C, amounting to approximately 360 PJ/year. This accounts for one-third of the total waste heat potential and is available across various industries such as chemicals, non-metallic minerals, food and paper. In the temperature range of 200-500 °C the amount of available waste heat has reduced to around 281 PJ/year. Industries utilizing high-temperature process heat, such as the steel industry, dominate the waste heat potential above 500°C, contributing to a substantial total potential of 446 PJ/year. The waste heat potential below 100°C is remarkably low, estimated at 4.5 PJ/year compared to other temperature levels. This can be attributed to the small temperature difference with the ambient temperature, minimal heat consumption within this range, and reduced heat losses (Papapetrou et al., 2018).

In total, the waste heat potential in the EU amounts to 1095 PJ/year, which represents 16.7% of the industrial consumption for process heat and corresponds to 9.5% of the overall industrial energy consumption (Papapetrou et al., 2018). These findings highlight the significant potential for utilizing waste heat as a valuable energy resource within the industrial sector, contributing to energy efficiency and sustainability goals.

2.1. Steel Industry Processes

Among the different industries, the iron and steel sector holds the most commanding position in terms of energy consumption. The making of steel includes several essential processes, beginning with the procurement of materials required for steel production. Iron ore, natural gas, limestone, oxygen, and coal are among the key materials used to create coke, sinter, and pellets. The sinter and pellets are agglomerated forms of iron ore which form the bases of the steel that is to be produced in the steel furnaces. The coke acts as a fuel source in the blast furnace and electric arc furnace. During combustion, coke facilitates the removal of oxygen from the iron ore, resulting in the production of pure iron.

Focussing on steel production the Netherlands, TATA Steel reported an annual energy usage of 230 PJ and CO_2 emissions of up to 6.5 Mton in the year 2017 (Daniels et al., 2019), a breakdown of this energy flow can be found in Figure 4. Although the sinter plant utilizes only a fraction of the total energy input, the amount of energy it consumes is still considerable in absolute terms.

The applicability of packed bed thermal storage systems in industrial processes depends on the nature of the process. While packed bed thermal storage can offer numerous advantages, it is particularly suited for batch processes that involve charging during periods of excess heat and discharging during times of heat demand. With storage times that typically have durations of a single day. Additionally, packed bed thermal storage systems can most effectively utilized for processes that output gaseous flows that can directly be led through the packed bed.

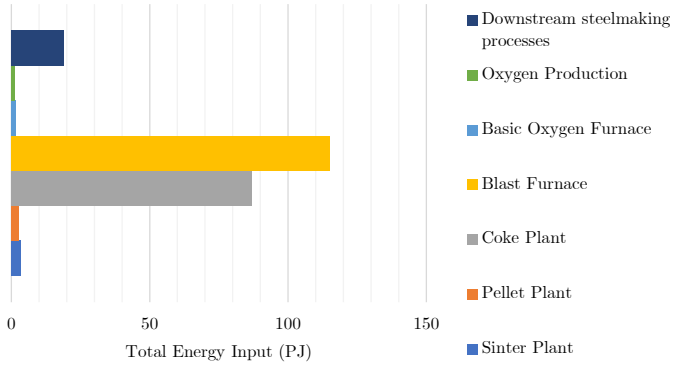

Figure 4: Overview of the total energy consumption of TATA Steel in the year 2017, with a breakdown of energy consumption for each process involved in the steelmaking operations (Daniels et al., 2019).

In some of the steel making processes, such as the one in the blast furnaces, heat recovery from gaseous streams is already implemented using regenerators known as Cowper heaters. Similarly, combustion gases in coke ovens are directed through regenerators for heat recovery. However, the coke oven product gas, containing high levels of pollutants like tar, cannot be effectively utilized. Alternatively, heat extraction from coke can be achieved through dry quenching, which generates hot air. The temperature of this gas flow greatly exceeds the envisioned maximum storage temperature of 500°C however. Harnessing this heat flow would necessitate the integration of a heat exchanger or the blending of the gas with colder air. Gases produced in the Basic Oxygen Furnaces are currently recovered only to a limited extent and have an intermittent nature, but these gas flows also exceed the 500°C limit, necessitating the implementation of a cooling process. In the steel rolling process, the hot steel sheets are typically cooled using water spray systems, harnessing useful energy from this cooling process is challenging. Regarding the slag (a metal type byproduct) generated from blast and basic oxygen furnaces, while it contains significant heat content, the slag itself can be considered a form of sensible heat storage in a solid. Therefore, the direct application of packed bed storage in this context is not apparent.

Two additional processes that can be considerate for heat recovery are the sintering and pellet production processes. Of particular interest is the heat that can be extracted from the sinter cooler as it exhibits the desired temperature range and has an extended heat release duration. Packed bed thermal storage systems rely on the capability to store heat for prolonged periods and gradually release it as needed. The sintering processes offers a prolonged heat soak period and the required conditions for thermal storage in a packed bed system. Therefore, the characteristics of the sintering application are considered to further analyse the feasibility of a heat storage system.

2.2. Sintering Waste Heat Potential

In the process of sintering, iron ore fines are mixed with other materials such as coke breeze and limestone to form a homogeneous mixture. This mixture is heated to a high temperature in a sintering plant, causing the particles to fuse together and form a porous mass. This porous mass, called sinter, is then cooled by blowing air through the pores. After the cooling process the sinter is broken down into smaller particles for use in the blast furnace. The exhaust gasses and hot air generated by the cooling process are often released to the environment, which is also the case at TATA Steel. Analysis of the energy flows within TATA Steel, as depicted in Figure A.17, reveals that no heat from the sinter plant is currently being recycled or utilized. Despite the current practice of releasing this heat into the atmosphere, it possesses significant potential for storage within a thermal storage system. This stored heat can on a later moment be used to re-heat the steel for subsequent processes.

In 2017, TATA Steel IJmuiden produced 3.74 Mton of sinter, resulting in a total energy usage of 3.31 PJ. The energy output balance of the sinter plant is illustrated in Figure 5.

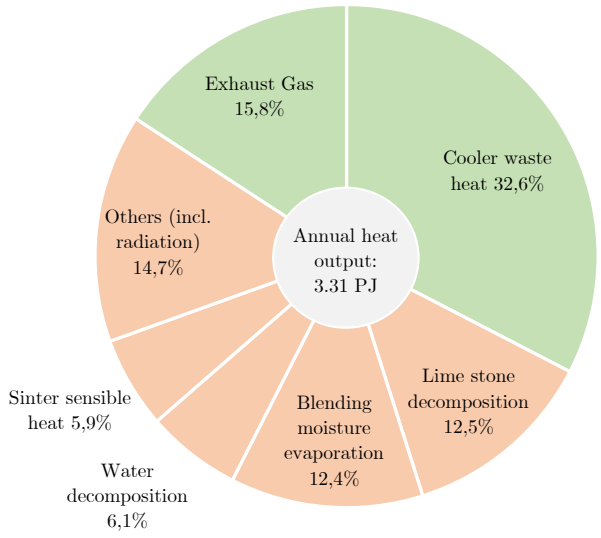

Figure 5: Heat output balance of sinter plant: Green sections indicates heat streams that could potentially be stored in a PBTS system and red sections indicate heat streams that are used in the chemical reaction or are wasted to the environment (Tanaka, 1979).

The data presented in this chart demonstrates that out of the total energy input into the sintering process, 15.8% is released as hot exhaust gases from the sinter while it is being heated. Additionally, 32.6% corresponds to the hot air being released by the sinter cooler. These two streams of heated fluids are well-suited for utilization within a packed bed storage system. The remaining energy, which comprises 51.6% of the total, is utilized for the chemical reactions taking place within the process, or it is dissipated as radiation or sensible heat within the sinter or the infrastructure of the sinter plant (Daniels et al., 2019).

The quality of the heat coming from the sinter cake cannot be determined from this data. Upon closer examination of the sintering process, it becomes evident that the temperatures of the hot air discharged from the sinter bed and the sinter cooler

are not evenly distributed over the length of the production line, as can be seen in Figure 6. Meaning the hot air coming from the beginning of the sinter cooler has a higher temperature then at the end of the sinter cooler due to the simple fact that the sinter is cooling down. The opposite is true for the heating of the sinter, where the highest temperature airflow is found at the end of the sintering machine. The heat flow characteristics of the sintering machine reveal a peak at the end of the process where the final sinter temperature reaches approximately 450°C. Within the sinter cooler section, the temperature of the air gradually decreases from around 550°C to 400°C within the initial third of the sinter cooler bed. If the packed bed storage system is to be heated by a uniformly high temperature heat flow, only a portion of the heat can be effectively utilized (see green zones). By recirculating the hot air through the bed, it is possible to enhance the heat recovery efficiency. Nevertheless, approximately 40-45% of the thermal energy can be effectively used to generate the desired 500°C airflow through the packed bed.

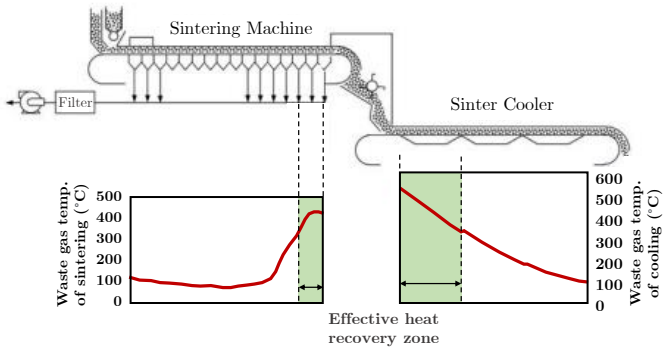

Figure 6: Schematic representation of the sinter plant. The sintering machine facilitates the heating of raw materials to produce sinter. The sinter cooler cooles the sinter by blowing cold air through the pores of the sinter.The red line indicates the temperature distribution of hot air coming from the sinter plant and the green regions indicate the usable temperature range (Steelplantech, 2013).

In order to determine the available charging time for the PBTS system to reach full capacity the duration of a sinter batch must be determined. Despite extensive research, no reliable data on the typical batch duration has been found. Consequently, the assumption is made that the sinter plant operates for a duration of ten hours per batch. Based on the previously presented data, it is possible to estimate the waste heat storage requirement. This estimation yields a total energy storage demand of approximately 1.1 TJ within the designated duration of the sinter batch.

3. Models and Assumptions

There are several model types that can be used to predict the behaviour of the PBTS systems, each providing different levels of detail. The basis of each model is a set of convection diffusion equations describing the heat transfer processes. These partial differential equations are solved by discretization to display how the temperature profile evolves in the tank.

3.1. Model Classification

Numerical models have different degrees of complexity and can be classified according to two important properties: the dimensions of the storage tank and the amount of material phases.

As is generally known, there are three spatial dimensions. The models can be distinguished according to the amount of dimensions considered.

1. 1D models: One-dimensional models assume that the thermal behaviour of the system is uniform and occurs in one spatial dimension, typically the axial direction. This model type is the most simple and computationally efficient.
2. 2D models: Two-dimensional models assume that the thermal behaviour of the system is a function of two spatial dimensions, typically the axial and radial direction, making this an axissymmetric problem.
3. 3D models: Three-dimensional models are the most detailed model type, assuming that the thermal behaviour of the system is a function of each spatial dimensions. Three-dimensional models provide the most detailed information, but are also the most computationally intensive.

Furthermore a distinction can be made between single and multi-phase models. The amount of phases indicate how many different temperatures profiles are computed.

1. Single-phase models: Single-phase models compute a single equivalent temperature for the fluid and solid phase. These models are suitable for studying systems with relatively low flow rates and small temperature differences.
2. Multiphase models: Multiphase models are used to simulate the heat transfer through multiple phases. This allows a distinction to be made between the temperature of the heat transfer fluid and solid particles, but also the temperature of the storage tank wall for example.

3.2. Common Modelling Assumptions

The following list presents some typical assumptions that are found in existing numerical models presented in Section 3.3.

1. The solid storage particles are considered as a homogeneous, porous medium and are not modelled as unique independent particles with varying dimensions.
2. Heat transfer fluid diffusers or distributor fins are not included in the models. This assumption is only of importance for multi-dimensional models.
3. The temperature of the solid medium is considered to be uniform. This signifies a Biot number (see, Section 5.3) below the conventional limit of Bi<0.1.
4. Volume changes in the solid or fluid phase due to variations in temperature are neglected.
5. The radiative heat transfer is often neglected due to its relatively small contribution to the overall heat transfer within the packed bed.
6. The temperature of the in-flowing HTF is considered to be constant.

3.3. Existing Numerical Models

Extensive research has been conducted on the modelling approaches for PBTS systems. A comprehensive work that presents multiple suitable models for heat storage systems is the study by Ismail and Stuginsky Jr (1999). Additional insights on differentiating factors were obtained from Avallone (2018) and Odenthal et al. (2019). In general, these models can be categorised into two groups. The first group comprises single-phase models that describe the thermal behavior using a single partial differential equation. The second group consists of two-phase models, employing two coupled partial differential equations to separately represent the fluid and solid temperatures. The latter group can be further subdivided into three fundamental models: the Schumann model, the continuous solid phase model, and the concentric dispersion model. The forthcoming review focuses exclusively on one-dimensional models, examining various approaches and methodologies.

Single Phase (1D-1P)

Single-phase models are advantageous for examining fixed beds where the thermal conductivity and thermal capacity of the solid material are significantly higher than those of the working fluid. In such scenarios, the temperatures of the solid and fluid phases are equivalent at any given point in time (Ismail and Stuginsky Jr, 1999). This models implements all the assumptions described in Section 3.2 and is governed by the following equation:

$$(\rho c_p)_{eff}\frac{\partial T}{\partial t} + \epsilon(\rho c_p)_{eff} v\frac{\partial T}{\partial x} = k_{eff}\frac{\partial^2 T}{\partial x^2} + h_{ext}\frac{A_{w\leftrightarrow ext}}{V_w}(T - T_{ext}) \tag{1}$$

Where T is the equivalent temperature of the solid and fluid phase; $(\rho c_p)_{eff}$ is the effective volumetric heat capacity of both phases; $\epsilon = \frac{V_f}{V_{tot}}$ is the porosity of the packed bed; v is the velocity of fluid across the packed bed; k_{eff} is the replacement conductivity of both phases; h_{ext} is the convective heat transfer coefficient with the exterior; $A_{w\leftrightarrow ext}$ is the outside area of the tank and V_w is the volume of the tank wall. Expressions for the effective volumetric heat capacity, velocity and effective conduction can be found in Appendix B.

The governing equation comprises several terms. The first term represents the internal energy of the system changing over time. The second term characterizes the internal energy associated with fluid flow, specifically describing the advancement of the thermocline within the tank. On the right-hand side, the third term accounts for the heat exchanged through conduction, it indicates the rate at which the temperature smears out across the tank. Finally, the last term quantifies the heat dissipated to the environment through convection.

T.E.W. Schumann (1D-2P)

One of the first mathematical solution to the problem of heat transfer from a liquid to a packed bed during the process of heating or cooling was formulated by (Schumann, 1929). His work, presented an analytical approach to the problem and did not delve into the experimental application of the theory presented. Opposed to the single phase model, a distinction is now made between the fluid and solid temperature and are both described with their own partial differential equation. In addition to the described simplifying assumptions, Schumann also neglected the heat losses to the environment in his model. Schumann characterised the thermal system by the following set of equations:

$$\begin{cases} \epsilon(\rho c_p)_f\left(\frac{\partial T_f}{\partial t} + v\frac{\delta T_f}{\delta x}\right) = h(T_s - T_f) \\ (1-\epsilon)(\rho c_p)_s\frac{\partial T_s}{\partial t} = h(T_f - T_s) \end{cases} \tag{2}$$

This 1D-2P representation of the thermal energy storage system is recognised for its simplicity and serves as the foundational framework for subsequent models aiming to capture this phenomenon. Notably, the governing equations differ from those for the single-phase case. A key distinction is the absence of a spatial derivative in the equation governing the solid phase, as the solid medium remains stationary unlike the fluid. Moreover, both equations lack a second spatial derivative, indicating that conduction within the solid and fluid phases is not considered. On the right-hand side, the term referred to as the source term governs the convective heat transfer between the fluid and solid states.

Continuous Solid Phase (1D-2P)

The continuous solid phase (CSP) model is in essence a combination of the presented single phase and Schumann model. It takes the complexity of the single phase equation and applies it to both differential equations. It assumes separate temperatures for both phases, with heat transfer between them typically determined using a lumped heat transfer correlation. It considers heat exchange by conduction and heat loss to the surroundings. The governing energy equations are as follows:

$$\begin{cases} \epsilon(\rho c_p)_f\left(\frac{\partial T_f}{\partial t} + v\frac{\partial T_f}{\partial x}\right) = k_{f,eff}\frac{\partial^2 T_f}{\partial x^2} + \\ \qquad h(T_s - T_f) + h_w\frac{A_{f\leftrightarrow w}}{V_w}(T_w - T_f) \\ (1-\epsilon)(\rho c_p)_s\frac{\partial T_s}{\partial t} = k_{s,eff}\frac{\partial^2 T_s}{\partial x^2} + \\ \qquad h(T_f - T_s) + h_w\frac{A_{s\leftrightarrow w}}{V_w}(T_w - T_s) \end{cases} \tag{3}$$

The continuous solid phase model is widely employed in the literature to characterize PTSB systems. Numerous studies have utilized this model to investigate various aspects of PTSB performance. For instance, Hoffmann et al. (2016) compared it to a single phase model; Yang et al. (2012) used it to study the performance of fictive storage material and Niedermeier et al. (2018) to compare the performance of a molten salt packed bed to a sodium packed bed. Additionally the model the model can be expanded by adding a third phase, explicitly describing the temperature in the wall of the tank to make the model more complex.

Concentric Dispersion (1D-2P)

A more sophisticated approach is the utilization of a dispersion concentric model (CD). It assumes a thermal gradient in-

side the solid particles. The proposed model partitions the storage tank into layers, each with a thickness equal to the diameter of the particles. It then computes the temperature distribution within each particle for every subsequent layer (Chekifi and Boukraa, 2023). The solids within the system exhibit symmetry conditions at their core, and the heat transfer coefficient is assumed to be uniform around each solid particle. These assumptions are represented by Neumann boundary conditions, establishing a coupling between the fluid and solid phases at the boundary interface (Handley and Heggs, 1969).

$$k_s \left(\frac{\partial T}{\partial r} \right)_{r=R} = h(T_s - T_f) \tag{4}$$

Within this model, the energy equation for the fluid phase largely retains its original form as outlined in Equation 3a. The distinction being that solid temperature in the last term is evaluated at the particle boundary $T_s|_{r=R}$ instead of the uniform particle temperature T_s, thereby establishing a coupling between the fluid and the following solid phase temperature expression:

$$(\rho c_p)_s \frac{\partial T_s}{\partial t} = k_s \left(\frac{\partial^2 T_s}{\partial^2 r} + \frac{2}{r} \frac{\partial T_s}{\partial r} \right) \tag{5}$$

The use of the current model is recommended for systems characterized by higher Biot numbers as the temperature of a particle cannot be considered to be uniform. This is typically associated with large particle sizes or high convective heat transfer rates. Noteworthy studies that have applied this CD model include Zhang et al. (2019), Galione et al. (2015) and Niedermeier et al. (2018).

3.4. Model Results Comparison

Although there are many studies covering the numerical modelling of the PBTS system, only a few experiments have been done to compare the data. The three primary examples are the Promes-CNRS Laboratory demonstrator, The Sandia National Laboratory pilot and the Solar one power plant pilot. Among these, the Solar One pilot experiment bears the closest resemblance to the application examined in this study, as the tank exhibits a similar magnitude in terms of volume and a comparable (dis)charge time. The main differentiating factors are the use of sand to fill the void spaces between the larger diameter quartize particles and a smaller temperature span. The main characteristics of this experiment can be found in Table 1, the characteristics of the other two experimental setups can be seen in Table B.7.

In the study carried out by Hoffmann et al. (2016), the performance of both the single-phase and two-phase (CSP) model was compared with experimental data. The temperature evolution resulting from these models is depicted in Figure 7 at different time intervals. It is evident that the dissimilarity between both models is practically negligible, as the temperature exhibits only marginal variances of a few tenths of a degree at most. The disparity observed between the model and experimental results remains consistently small, with variations never exceeding a margin of four to five degrees. However, when comparing these results to the two experiments conducted on a smaller scale, there is a more noticeable disparity between the predicted and actual temperatures. The average mean errors with the experimental results for the smallest storage tank setup is reported as 1.75°C and 1.32°C and the maximum error as 7.7°C and 6.4°C for the 1D-1P and 1D-2P models respectively. For further details regarding the experimental setups and a comprehensive comparative analysis of the results from the other two experiments, refer to Appendix B.2.

Table 1: Experiment details and characteristics of the Solar One pilot (Hoffmann et al., 2016)

Parameter	Solar One pilot
Energy Capacity	612 GJ
Heat transfer Fluid	Caloria HT 43
Storage Material	Quartzite rock and sand
(Dis)charge time	8 h
Tank Height	12 m
Tank Diameter	18.2 m
Tank Volume	3122 m^3
Packed-Bed Porosity	0.22
Particle Diameter	0.46 cm
HTF Mass flow rate	23 kg/s
Hot Temperature	295.5°C
Cold Temperature	179.2°C

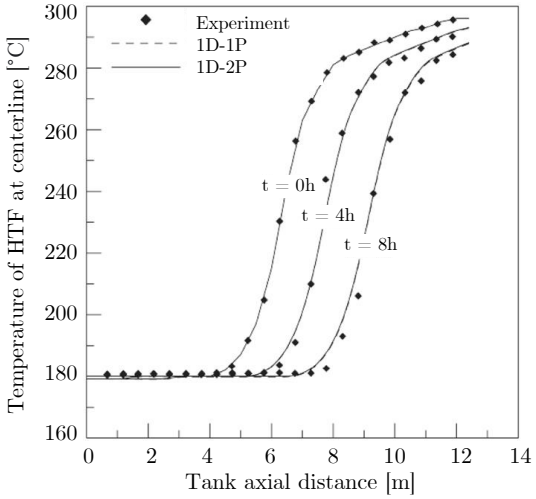

Figure 7: Comparison of data from the single and two phase (CS) model compared to experimental data from the Solar One pilot (Hoffmann et al., 2016).

4. Materials and System Characteristics

The subsequent section provides an overview of different heat transfer fluids suitable for transferring heat into the tank, as well as various types of rock solids capable of storing thermal energy. By considering the material properties and packing characteristics, the necessary storage volume can be deter-

mined, followed by the assessment of flow conditions based on specific tank dimensions.

4.1. Heat Transfer Fluid

The HTF is utilized to facilitate the transfer of heat into the solid storage material. During the charging phase, a heated flow is pumped from the top to the bottom of the tank, allowing the thermal energy to be absorbed by the solid medium. Conversely, during the discharging phase, a cold flow of the HTF is pumped from the bottom to the top of the tank, extracting the stored heat from the solid material. There are various heat transfer fluids that can be used in a the PBTS system. The selection of the heat transfer fluid depends on several factors, including the operating temperature range, the desired heat transfer rate, and the specific application requirements. Some of the commonly used heat transfer fluids for packed bed thermal storage systems are: air, molten salt and thermal oil. The properties and operating ranges of these materials can be found in Table 2.

Table 2: Operating range and material properties of four prominent heat transfer fluids at 300°C, namely: ambient air (van Esch, 2018), Therminol VP-1 thermal oil (Alami et al., 2018) and Solar salt consisting of 60% $NaNO_3$ and 40%KNO_3 (Mao et al., 2010).

Material	$T_{min/max}$	c_p	ρ	μ	k
Air	-	1046	0.61	3.0e-5	0.045
Oil	12 - 400	2314	817	2.2e-4	0.0964
Molten Salt	220 - 560	1495	1899	3.3e-3	0.45

The advantage of air is its unlimited availability, zero cost, and practically unrestricted operating temperature range. However, due to its relatively low density, a significant volume of air is required to transfer the desired amount of heat. On the other hand, molten salt and thermal oil offer the advantage of high heat capacity, allowing the same amount of heat to be transported with a reduced mass flow rate. A drawback of molten salt is its minimum operating range of 220°C, necessitating the incorporation of safety mechanisms, such as heat pumps, to prevent the molten salt from getting below this temperature and solidifying in the storage tank. Conversely, in the case of thermal oil, it is crucial to incorporate a cooling mechanism to prevent the fluid from exceeding its temperature limit of 400°C.

Another commonly used heat transfer fluid for low-temperature applications is water. However, due to the phase transition characteristics of water near the lower temperature limit and the potential for steam to generate high pressures within the packed bed, this particular heat transfer fluid is not further investigated in this study.

4.2. Solid Storage Material

There are several options available for solid storage media that can be used in a packed bed thermal storage system. This study will look at few prominent types of rock that are used in thermal storage systems. Rocks are generally known to have a high thermal conductivity and large thermal mass, and due to their wide availability are considered as an inexpensive and attractive option to store heat (Knobloch et al., 2022). Different types of rocks have slightly varying properties that influence the performance of the system. The rock types that will be considered in this study are concrete, granite and basalt. Their respective material properties are presented in Table 3.

Table 3: material properties of three prominent rock type solid storage media, namely: Concrete (Bejan, 1993), Granite (Miranda et al., 2019) and Basalt (Robertson, 1988).

Material	c_p	ρ	ρc_p	k	α
Concrete	920	2300	2.1e6	1.7	7.7e-7
Granite	720	2630	1.9e6	3.1	1.6e-6
Basalt	840	2900	2.4e6	3.0	1.2e-6

4.3. Sphericity

The sphericity of a particle is a measure of how closely a particle's shape resembles a perfect sphere. The higher the sphericity, the more uniform the packing of particles. If the particles are not spherical, they tend to pack more loosely, creating larger voids. This results in a lower surface area available for heat transfer. In contrast, when spherical particles are used in a packed bed thermal storage system, they pack more tightly, resulting in smaller voids and a higher overall contact area between the particles. This leads to a higher thermal conductivity, allowing for faster heat transfer within the system (Fei et al., 2019).

In reality, a batch of rocks that would be used to create the packed bed would never contain perfectly spherical particles. Figure 8 gives a visual indication of the sphericity of a sub-rounded particle. As all mathematical relations assume a perfectly spherical particle, a sphericity of one is used for the remainder of this study.

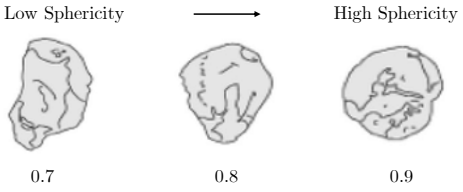

Figure 8: Indication of sphericity for sub-rounded particle (Ulusoy, 2019)

4.4. Porosity

Porosity, or void fraction, refers to the ratio of empty volume within the bed to the total volume of the bed.

$$\epsilon = \frac{V_f}{V_{tot}} \tag{6}$$

Where ϵ is the volume fraction that is occupied by the fluid; V_f is the volume occupied by the fluid and V_{tot} is the total volume of the packed bed.

The porosity of a packed bed thermal storage system determines the amount of fluid that can flow through the bed

and thus the rate at which heat can be transferred between the fluid and the storage medium. A higher porosity means there is more space between the solid particles, which allows for greater fluid flow and potentially more heat transfer. However, a higher porosity also means that there is less solid material to store heat. Dependent on the selected heat transfer fluid, this can strongly influence the overall thermal capacity of the system.

The optimal porosity strongly depends on the application of the thermal storage system. As the selected application prioritises long-term heat storage over rapid heat transfer, a lower porosity could be beneficial as there is more solid material available to store heat. This does, however, come with the drawback of higher frictional pressure losses during charge and discharge operations, necessitating a greater amount of pumping power, as is further discussed in Section 6.

Several studies have analysed the porosity of a packed bed based on varying particle shapes and sizes. As a result, the following relation has been derived to estimate the mean void fraction of particles with a constant sphericity (Benyahia and O'Neill, 2005).

$$\epsilon = \left(0.1504 + \frac{0.2024}{\psi}\right) + \frac{1.740}{\left(\frac{D}{d} + 1.140\right)^2} \tag{7}$$

Where ψ is the sphericity of the particle; D is the diameter of the storage tank and d is the diameter of a single particle in the packed bed.

The relationship between porosity and tank-to-particle diameter ratios is demonstrated in Figure 9, revealing an exponential decline as the ratio increases. Once the ratio surpasses twenty, the porosity stabilises at an equilibrium value. A lower sphericity leads to increased porosity, consequently creating larger voids between the particles. Specifically, at a sphericity of one, the porosity reaches 0.35 for sufficiently high ratios.

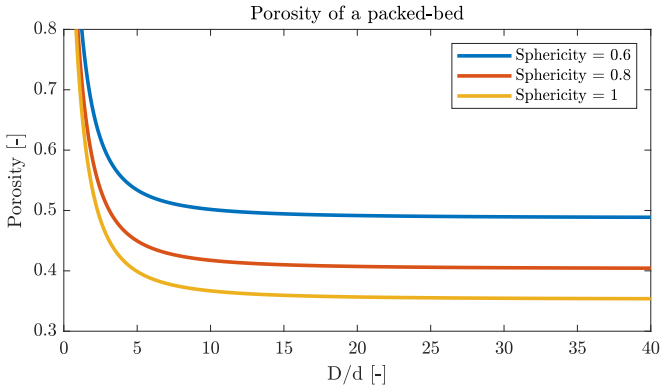

Figure 9: Porosity for a wide range of tank- to particle diameter ratios according to Equation 7. Each line represents the porosity for different sphericity particles.

4.5. Packed-Bed Size

Once the characteristics of the particles have been set, the volume of the packed bed and the size of the storage system can be determined. This is done using the properties of the storage materials, the operating temperature range and the desired amount of thermal energy that is to be stored in the system. As discussed in Section 2.2, the thermal storage system needs to accommodate 1.1 TJ of thermal energy. To determine the required volume of the packed bed, the following formula can be utilized:

$$V = \frac{Q}{(\rho c_p)_{eff} \Delta T} \tag{8}$$

where V is the required volume of the storage tank; Q is the amount of thermal energy that needs to be stored and ΔT is the temperature span of the heat transfer fluid.

Assuming the tank diameter to particle diameter ratio is sufficiently large the porosity can be taken as $\epsilon = 0.35$. The temperature difference between the charged and discharged state of the system is ΔT = 500 - 100 = 400°C for air, ΔT = 500 - 220 = 280°C for molten salt and ΔT = 400 - 12 = 388°C for thermal oil. The specific energy capacity of the solids and transporting fluids are given in Table 3 and Table 2. The resulting storage volume for the different combinations of storage media are presented in Table 4.

To get an indication on the dimensions of the storage system for the required storage volume, Equation 9 can be used. This relation finds the dimensions of the cylindrical storage such that the diameter and height are equal. The resulting surface area of the tank would be minimal for the given volume which leads to the smallest energy losses to the environment. The resulting dimensions for a minimal surface area can be found in Table 4.

$$D_{min,area} = H_{min,area} = \left(\frac{4V_t}{\pi}\right)^{\frac{1}{3}} \tag{9}$$

Upon reviewing Table 4, it becomes evident that for the implementation of this system, the approximate volume of the storage tank should fall within the range of 1250 to 2250 m^3, depending on the combination of HTF and storage media. Consequently, the resulting tank dimensions would be approximately 12 to 14 meters in both diameter and height.

Table 4: The required storage volume and the resulting dimensions of the storage tank, with equal diameter and height, for various combinations of storage media. A particle diameter of 0.1 m was selected, but the particle diameter showed to have minimal effect on the presented values.

Volume & Size	Air	Molten Salt	Thermal Oil
Concrete	2000 m^3 & 14m	1650 m^3 & 13m	1400 m^3 & 12m
Granite	2250 m^3 & 14m	1750 m^3 & 13m	1500 m^3 & 12m
Basalt	1750 m^3 & 13m	1500 m^3 & 12m	1250 m^3 & 12m

4.6. HTF Mass Flow

Knowing the amount of thermal energy that needs to be stored within the estimated ten hour time frame of the sinter batch, it is possible to calculate the required mass flow rate of the heat transfer fluid through the PTSB system in order to store all the energy. Given the specific heat of the HTF, the required mass flow is computed as:

$$\dot{m} = \frac{q}{c_p \Delta T} \tag{10}$$

Where q is the amount of energy that enters the system every second. It is found by dividing the total amount of energy that must be stored by the time span of the sinter batch and results in a value of 30.3 MW.

The computations reveal that the desired mass flow rate for both air and molten salt is precisely 72 kg/s. This outcome arises from the fact that while molten salt exhibits a higher specific heat, air possesses a broader temperature operating range, which eventually results in an identical mass flow. For thermal oil the required mass flow is found to be around 34 kg/s. Subsequently the required flow velocity of the HTF can be found. A distinction can hereby be made between the effective flow velocity and superficial velocity. The effective velocity describes the velocity through the bed while accounting for voids through which the fluid can flow (Equation 11). The superficial velocity describes the velocity of the HTF as if the tank would be empty and the fluid could freely flow through the complete cross-section (Equation 12).

$$v = \frac{\dot{m}}{\rho \epsilon A_t} \tag{11}$$

$$v_{sf} = \frac{\dot{m}}{\rho A_t} \tag{12}$$

Where A_t is the cross-sectional area of the tank.

In both cases the resulting flow velocity varies widely depending on the selected storage tank dimensions. For now only the flow velocity for the minimal heat loss tank are considered ($D = H$), these can be found in Table 5 for the various combinations of storage media. The analysis indicates that the typical flow velocity of air ranges from 2.1 m/s to 2.5 m/s, whereas the flow velocity of molten salt and thermal oil is considerably lower, averaging at 8.4e-4 m/s and 1.0e-3 m/s respectively. This large difference can be attributed to the significantly greater density of molten salt and thermal oil, which is approximately three thousand times larger than air. This allows it to carry a larger amount of heat with only a fraction of the volume.

5. Classifications

Two relevant dimensionless numbers to be studied are the Biot number and Fourier number as they can tell something about characteristic temperature, time- and length scales. Since these dimensionless numbers have dependencies with the Reynolds and Nusselt number, they will also briefly be discussed.

Table 5: The resulting effective velocity thought the packed bed if all energy from the sinter plant is to be stored in the tank. Again a particle diameter of 0.1 m was selected, but the particle diameter showed to have minimal effect on the presented values.

Flow Velocity	Air	Molten Salt	Thermal Oil
Concrete	2.3 m/s	8.4e-4 m/s	1.0e-3 m/s
Granite	2.1 m/s	8.0e-4 m/s	9.7e-4 m/s
Basalt	2.5 m/s	8.9e-4 m/s	1.1e-3 m/s

5.1. Reynolds Number

The Reynolds number is used to predict the flow regime in a fluid system. For a packed bed the flow regime is considered laminar for Re < 10 and turbulent for Re > 1000. The Reynolds number is computed as follows:

$$Re = \frac{\rho d v}{\mu} \tag{13}$$

Where v is the effective velocity of the fluid and μ is the viscosity of the fluid.

The calculations reveal that the Reynolds number for the air flow would result in approximately 2500, while for the molten salt and oil flow, this would be around 25 and 200 respectively. Consequently, the air flow can be characterized as turbulent, while the molten salt and oil flow is in a transitional state between laminar and turbulent regimes.

5.2. Nusselt Number

The Nusselt number characterizes heat transfer between a fluid and solid surface, influenced by fluid properties and flow conditions. The Nusselt number is expressed as:

$$Nu = \frac{h L_{c,Nu}}{k_f} \tag{14}$$

Where $L_{c,Nu}$ is the characteristic length of the hydraulic radius.

Given the challenge of accurately describing the complex relationship of a flow problem, empirical relations are used to obtain numerical values for the Nusselt number. Various empirical relations exist for PBTS systems, offering slightly different expressions. For the studied case, the Nusselt relation from Whitaker (1972) is found most fitting (Equation 15).

$$Nu = (0.5 Re^{1/2} + 0.2 Re^{2/3}) Pr^{1/3} \tag{15}$$

Figure 10 shows how the presented Nusselt expression related to several other, often used relations. The plot reveals that, at lower Reynolds numbers, the disparities among the different relations are relatively small. However, as the Reynolds numbers increase, the variation in Nusselt numbers becomes more pronounced. The Nusselt relation proposed by Whitetaker was chosen based on its alignment with the desired application's experimental parameters and it proves to be the average of the other relations.

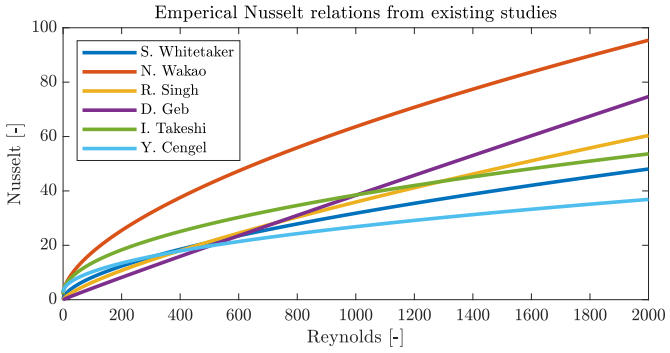

Figure 10: The Nusselt number as a function of a wide range of Reynolds numbers for several existing empirical relations (Whitaker, 1972), (Wakao et al., 1979), (Singh et al., 2006), (Imai et al., 1994), (Cui et al., 2012) and (Yunus Cengel et al., 2018). A Prandtl number of 0.7 (characteristic for air flow) was selected. The relation that was used during this study is indicated in blue.

The Nusselt number can be used to determining convective heat transfer coefficient. According to Whitetaker, the appropriate length scale is six times the hydraulic radius of a particle. Note that the wetted surface of the tank wall is neglected relative to the wetted surface of solid particles. The length scale is expressed as:

$$L_{c,Nu} = 6\left(\frac{V_p}{A_p}\right)\frac{\epsilon}{1-\epsilon} \tag{16}$$

Where V_p is the volume of a single particle and A_p is the area of a single particle.

Upon substituting the appropriate numerical values, the resulting convective heat transfer coefficient for ten centimeter diameter particles are 46 W/(m^2 °C) for air flow, 65 W/(m^2 °C) for molten salt flow and 44 W/(m^2 °C) for thermal oil flow. It was found the convective coefficient could approximately be related to particle diameter as: h $\propto$ d$_p^{-0.4}$.

5.3. Biot Number

The Biot number relates the resistance to heat transfer within a solid object to the resistance at the surface through which heat is exchanged with the surrounding fluid. Mathematically the Biot number is defined as:

$$Bi = \frac{h_f L_{c,Bi}}{k_s} \tag{17}$$

Where the characteristic length of the particle is often taken as the particle radius for transient heat transfer problems (generally Bi >> 1) and taken as the particle volume to area ratio for lumped capacitance methods (generally Bi < 0.1). A full derivation of this lumped capacitance length scale can be found in Appendix C.

In Figure 11, a visual representation showcases the typical temperature drop in both the fluid and solid phases for different Biot number ranges at the initial time moment. It is evident that for very low Biot numbers (Bi << 1), the temperature drop in the solid remains relatively small and the particle temperature is assumed to be uniform. For higher Biot numbers (Bi >> 1) the temperature drop in the solid becomes more substantial. For these cases the heat equation must be solved to determine the time-varying temperature distribution within the solid. When the Biot number approaches one, the temperature difference between the fluid and solid phases equalise. Under the flow conditions presented in Section 4.6 it was found the lumped capacitance method can typically be applied for particle diameters of two centimeters and lower for all material combinations, whereas transient temperature must be considered for diameters above that.

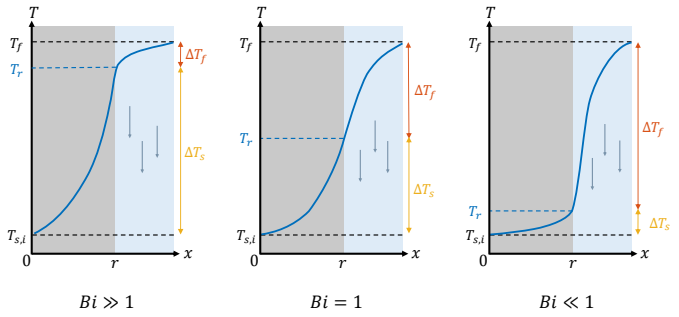

Figure 11: Illustration of typical temperature gradients in fluid and solid phase for the three Biot regimes. The grey area represents the solid particle and the light blue area represents the flowing fluid. The blue line indicates the approximate temperature profile.

5.4. Fourier Number

The Fourier number characterises the temperature response of a material subjected to heating or cooling and is mathematically expressed as:

$$Fo = \frac{\alpha t}{r^2} \tag{18}$$

Where α is the diffusivity of the solid particles which is computed as $\alpha = \frac{k_s}{(\rho c_p)_s}$; t is the time and r is particle radius.

The Fourier number can be interpreted by considering a cool particle surrounded by a hot convective environment, in this case the HTF. When the Fourier number is small (Fo << 1), it indicates that the particle's core has not yet 'noticed' the temperature increase, and the majority of temperature change occurs primarily at the outer edge of the particle. In contrast, when the Fourier number is large (Fo >> 1), sufficient time has passed to approach a steady-state situation, and the particle tends to reach a uniform temperature distribution throughout its volume.

5.5. Particle Charge

For Biot numbers greater than one the non-uniform temperature distribution within the particle can be solved with the heat

equation, which can be found in Appendix C. An accurate approximation solution for the temperature distribution within a spherical particle is presented as follows:

$$\theta = A_1 e^{-\lambda_1^2 Fo} \frac{sin(\lambda_1 r/r_0)}{\lambda_1 r/r_0} \tag{19}$$

Where θ is the dimensionless temperature within the particle and A_1 and λ_1 are constants. The values of these constants depend on the Biot number and can be found in Table C.8.

This equation can be applied for spherical particles with a surface temperature corresponding to the temperature of the convective environment. For this case the convective flow and particle surface have a temperature of 500°C whilst the core of the particle has a initial temperature of 100°C. Figure 12 shows the temperature profile in the particle for different time moment. In the graph, the left side corresponds to the particle's core, while the right side represents its surface. As can be observed, as time progresses the temperature at the particle core approaches the surface temperature of the particle.

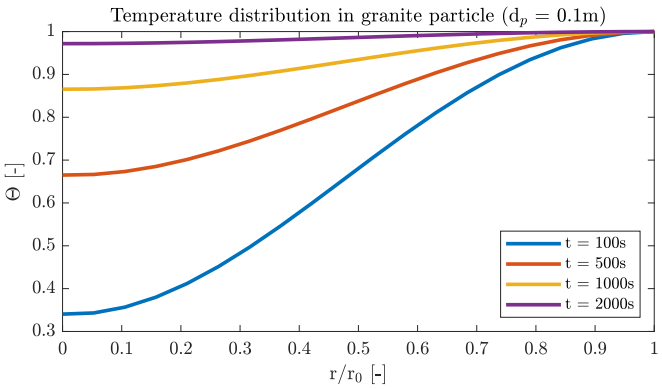

Figure 12: Characteristic temperature distribution in granite particle (d_p = 0.1 m) for Biot numbers greater than one (transient temperature) at different moments in time. The particle is surrounded by a 500°C air flow whilst the initial particle core temperature is 100°C.

A similar approximate solution with the same initial conditions can be used to derive the duration necessary to heat up the particle to a specific level of charge. For a sphere this expression is given as:

$$\frac{Q}{Q_{max}} = 1 - \theta_0 \frac{sin(\lambda_1) - \lambda_1 cos(\lambda_1)}{\lambda_1^3} \tag{20}$$

Where θ_0 is defined as the dimensionless temperature at the particle core and can be found by reducing Equation 19 to:

$$\theta_0 = A_1 e^{-\lambda_1^2 Fo} \tag{21}$$

To verify the reliability of this method, a comparison was made against results of existing literature. The results demonstrated a strong agreement. Further details regarding this validation can be found in Appendix C.3. Figure 13 depicts the duration required to heat up particles of varying diameters. Observing the graph, it becomes evident that particle size has a major influence charging times. A spherical granite particle with a diameter of one centimeter takes approximately 160 seconds to charge; a ten centimeter particle one hour and a particles with a diameter of half a meter may require up to eleven hours to fully saturate.

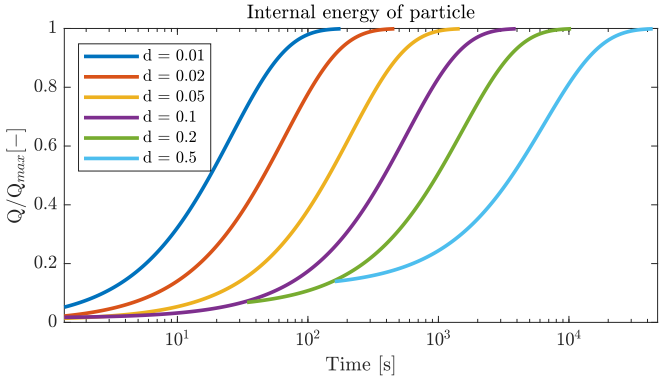

Figure 13: Time to charge different diameter granite particles for a constant 500°C air flow surrounding the particle.

The calculations were also performed for the flows of molten salt and thermal oil, using a ten centimeter diameter granite particle. The corresponding charging times for reaching 50% and 99% charge are presented in Table 6. The same analysis revealed that the charging times for Basalt and Concrete particles were approximately 20% and 30% longer respectively.

Table 6: Particle charge times in minutes for a granite particle with a ten centimeter radius in a 500°C convective environment. Charging times are presented for air, molten salt and thermal oil flows.

Particle Charge	Air	Molten Salt	Thermal Oil
50%	6 min	20 min	10 min
99%	60 min	130 min	65 min

6. Pressure Loss

Pressure loss occurs in a packed bed due to the resistance encountered by the fluid as it flows through the bed of particles. This resistance arises from various factors, such as the frictional interaction between the fluid and the particles and changes in flow direction. The Ergun equation is a widely used empirical correlation that quantifies the pressure loss in a packed bed. It relates the pressure drop to the fluid velocity and the various properties of the packed bed (Ergun, 1952):

$$\Delta p = \frac{150\mu L}{d^2} \frac{(1-\epsilon)^2}{\epsilon^3} v_{sf} + \frac{1.75 L\rho}{d} \frac{(1-\epsilon)}{\epsilon^3} v_{sf}^2 \tag{22}$$

Where μ is the viscosity of the HTF and L is the length of the packed bed.

The first term on the right-hand side of the equation represents the viscous resistance, which is dominant at low flow velocities and accounts for the frictional losses between the fluid and the packed bed. The second term represents the inertial resistance, which becomes significant at higher velocities and is related to the changes in flow direction and momentum transfer within the bed. Upon identification of the pressure drop over the packed bed, the power required to overcome that pressure drop can simply be found by multipliying it with the volumetric flow rate of the HTF as:

$$P = Q\Delta p \tag{23}$$

Where Q is the volumetric flow rate of the HTF.

Figure 14 depicts the pressure drop and corresponding pumping power requirements across the packed bed for a wide range of particle diameters. The graph clearly demonstrates an exponential decline in pressure drop with increasing particle diameter. This behaviour can be attributed to the denser packing of smaller particles at lower diameters, which results in a significant rise in viscous resistance due to the contact surface between the particles and the fluid. Furthermore, it is evident that the pressure drop for the molten salt and thermal oil flow is orders of magnitude lower. The higher density and viscosity of molten salt in comparison to air would suggest an increase in pressure drop, as indicated in Equation 22. However, due to the substantially lower flow velocity of molten salt the overall pressure drop strongly decreases. The air flow requires a substantial amount of pumping power to overcome the pressure drop. For one centimeter particles, the pumping power during charging amounts to approximately 6.7% of the total power entering the system. For particles with a diameter of ten centimeters, this value decreases to 0.5% and continues to decrease further for larger diameter particles.

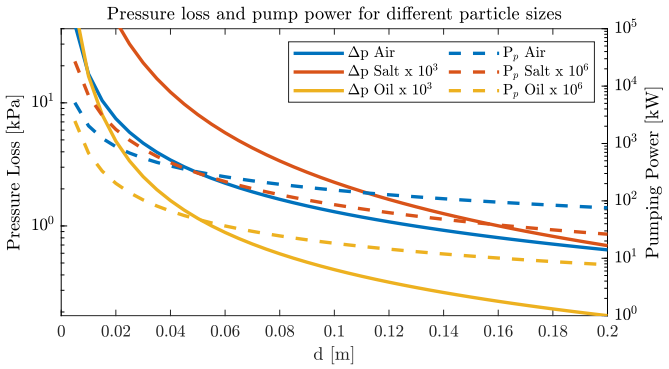

Figure 14: Pressure drop (straight line) and required pumping power (dashed line) across a packed bed composed of granite particles with a bed length of 14 m and a porosity of 0.35. The air, molten salt and thermal oil flow through the bed at a superficial velocity of 0.75 m/s, 2.8e-4 m/s and 3.4 m/s respectively.

Figure 15 illustrates the correlation between pressure loss and the associated pumping power for various tank shapes, while keeping the particle diameter constant. On the left side of the graph, a tank with twice the diameter relative to its length is represented, whereas the right side depicts a tank with twice the length compared to its diameter. As the diameter decreases, maintaining a constant volume flow rate necessitates an increase in flow velocity. Consequently, this increased velocity, in combination with an increase in tank length, gives rise to a larger pressure drop within the system. Once again, it is evident that the pressure drop and pumping power required for the molten salt and thermal oil flow is several orders of magnitude lower compared to air flow.

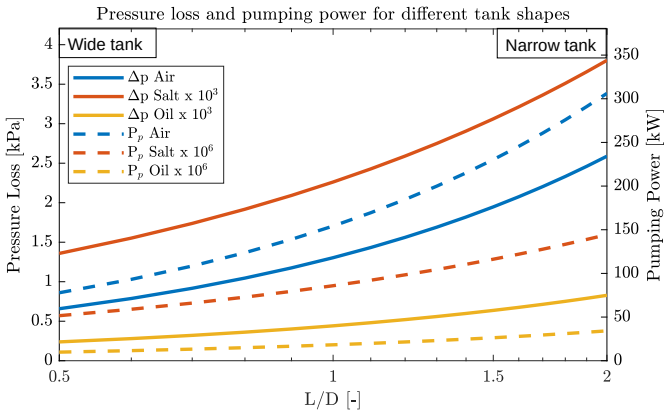

Figure 15: Pressure drop across a packed bed composed of granite particles. The diameter of the particles in the bed is ten centimeter; the length of the bed is 14 m and has a porosity of 0.35.

7. Thermocline Model

To simulate the temperature evolution and the propagation of the thermocline in the storage tank, a simplified numerical simulation was conducted. A continuous solid phase model (1D-2P) was chosen for the simulation, as presented by Equation 3, with the exclusion of heat loss to the environment. The governing equations that describe the fluid and solid temperature, respectively, are as follows:

$$\begin{cases} \epsilon(\rho c_p)_f \left(\frac{\partial T_f}{\partial t} + v\frac{\partial T_f}{\partial x}\right) = k_f \frac{\partial^2 T_f}{\partial x^2} + h(T_s - T_f) \\ (1-\epsilon)(\rho c_p)_s \frac{\partial T_s}{\partial t} = k_s \frac{\partial^2 T_s}{\partial x^2} + h(T_f - T_s) \end{cases} \tag{24}$$

To reduce computation time, a tank length of one meter was selected. The fluid and solid media are air and granite respectively and thermal physical properties are assumed to be constant throughout the simulation. A uniform temperature was assumed for the solid material, signifying Bi < 0.1.

7.1. Initial and Boundary Conditions

The simulation involves charging a packed bed from a lower temperature limit of 100°C using a hot flow of 500°C. The hot flow has a constant velocity of v=0.05 m/s and both the diffusivity of the solid and the fluid phase have a value of α=1e-5 m^2/s. The source term responsible for the transfer of heat

between the two phases has a value of one. Due to the one-dimensional nature of the model, there is a boundary condition for each phase at the top and bottom of the system. The hot HTF enters from the top of the tank, which establishes an input temperature condition (Dirichlet boundary condition), while an adiabatic condition is imposed for the solid phase (Neumann boundary condition).

$$T_f(x = 0) = 500 \tag{25}$$

$$\frac{\partial T_s(x = 0)}{\partial x} = 0 \tag{26}$$

The cold fluid exiting the tank has adiabatic conditions for both the fluid and the solid phases.

$$\frac{\partial T_f(x = L)}{\partial x} = \frac{\partial T_s(x = L)}{\partial x} = 0 \tag{27}$$

The numerical model was implemented using MATLAB software and solved utilizing the PDEPE solver. This solver employs a domain discretization technique and transforms the PDEs into ODEs to obtain the solution through a stepwise time-marching scheme. The maximum simulation time is sixty seconds and the spatial and time-intervals were choosen as Δx =1.6e-4 m and Δt =1.6e-3 s respectively.

7.2. Simulation Results

Temperature profiles resulting from the simulation can be observed in Figure 16. The graph shows the solid and fluid temperature at four time instances. As can be seen the system is completely charged after the maximum simulation time of sixty seconds.

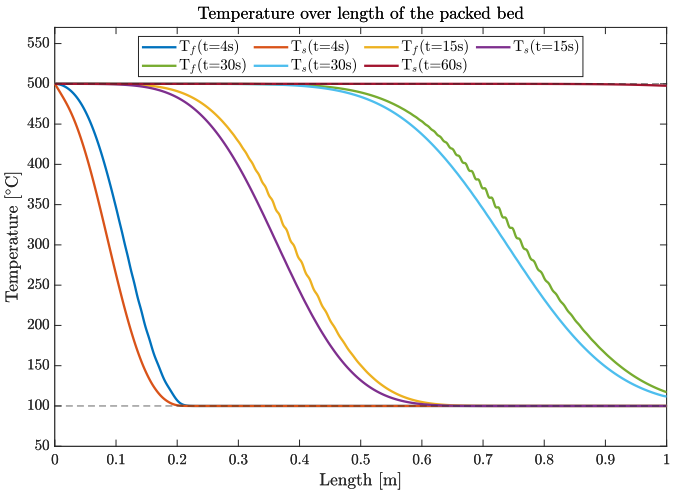

Figure 16: Resulting fluid and solid temperature profiles from the continous solid phase model. These profiles depict the temperature variations at three distinct time points. Notably, the final solid temperature profile indicates the system has reached full charge after a duration of sixty seconds.

A notable observation is that the solid temperature lags behind the fluid temperature. This is due to the fact that the system is in a charging state and it takes time for the HTF to transfer its heat to the solid. The rate with which this happens is governed by the source term, increasing this term would result in faster heat transfer and reduced temperature differentiation. Another trend that can be seen is the gradual reduction in the sharpness of the thermocline as time progresses. This is caused by the diffusivity term which gradually disperses the temperature and drives it toward uniformity throughout the entire tank. As the diffusivity increases, the sharpness of the thermocline would reduce more rapidly over time. The velocity of the heat transfer fluid governs the speed at which the heat front advances through the tank. A higher velocity would mean that the thermocline would move through the tank faster. Illustrative examples showcasing the impact of the aforementioned factors can be observed in Appendix D.

Following the simulation of a basic PBTS system, an attempt was made to simulate a system utilizing the thermo-physical properties of the HTFs and solid storage media as outlined in this study. However, the results obtained from this simulation proved to be unreliable and unsuitable for inclusion in the study.

8. Conclusion

The sintering process in the steel industry was selected as the application for the PBTS system. This process was found most suitable as the temperature of the outgoing waste heat flow corresponds to the maximum envisioned temperature of the system. The set point of this study was therefore to store the approximatly 1.1 TJ of energy that is released from the sinter plant in the PBTS system and do this within a ten hour timeframe. This results in charging power of 30.3 MW.

Through an extensive literature review, three distinct one-dimensional numerical models were identified for predicting the temperature behavior of the PBTS system. The selection of the appropriate model depends on specific requirements and system properties. A single-phase model is recommended when computational time is a priority over accuracy. However, this type of model may not be suitable for small storage systems (L < 2m) as temperature errors can be seven to eight degrees. This model does demonstrate high accuracy for larger systems exceeding a length of six meters. Multiple-phase models can be employed to describe both solid and fluid temperatures with greater precision, but they do not provide significant advantages for larger storage systems (L > 6m). Concentric dispersion models are preferable when a more detailed understanding of temperature gradients within particles at specific levels in the tank is desired.

Three different heat transfer fluids were investigated: air, molten salt, and thermal oil. Air offers the advantage of being cost-effective and having a wide temperature operating range. Molten salt and thermal oil have a more limited operating range, requiring temperature safety mechanisms, but excel in their ability to transport a large amount of heat in a given volume in comparison to air. This characteristic leads to smaller storage tank dimensions and reduced volume

flow rates required to store all the waste heat in the system. Typical storage volumes were observed to be the largest for air, averaging around 2000 m^3, followed by molten salt with approximately 1600 m^3, and thermal oil with the smallest volume of around 1300 m^3. For an optimal insulated tank design (D = H), the dimensions of the system were determined to range approximately from twelve to fourteen meters. To achieve complete heat storage within the designated timeframe, the required mass flow rates were found to be approximately 72 kg/s for both air and molten salt, while thermal oil only required 34 kg/s. As a result, there is a significant disparity in the required flow velocities, with air requiring roughly 2 m/s, and molten salt and thermal oil necessitating much lower velocities at approximately 8e-4 m/s and 1e-3 m/s, respectively. The characteristics of the solid particles also exert a minor influence, leading to slight differences in flow velocities.

Analysis of various dimensionless numbers revealed that the system exhibits different behaviours depending on the system properties, with the type of heat transfer fluid and its flow characteristics playing a significant role. Specifically, for air, the flow regime is predominantly turbulent, whereas for molten salt and thermal oil, the flow can be either laminar or in a transitional state. With the presented flow conditions the lumped capacitance method is generally applicable only for particle diameters below two centimeters. The heat transfer coefficient was found to have a strong correlation with the particle diameter in this system, following a proportional relationship as $h \propto d_p^{-0.4}$. Numerical methods utilizing the Fourier number were employed to estimate the charging time of solid particles in a convective environment. The results demonstrated that charging times increase exponentially with larger particle diameters. Moreover, it was observed that for the flow of molten salt, the charging time for a particle is approximately twice as long compared to air or thermal oil. The choice of solid material also influenced the charging time, with basalt exhibiting a 20% increase and concrete showing an even higher increase of 30%.

The pressure loss in the system exhibits a strong relationship with the selected particle diameter, with smaller particle diameters resulting in exponentially higher pressure losses. However, for particle diameters of ten centimeters or larger, the decrease in pressure loss becomes less significant. Notably, the flow velocities of molten salt and thermal oil are considerably lower, leading to negligible pressure losses and minimal required pumping power in the system. In contrast, for air flow, the required pumping power can reach up to 6.7% of the total input power for particles with a diameter of one centimeter, while it reduces to approximately 0.5% for particles with a diameter of ten centimeters. Larger diameter storage tanks exhibit lower pressure losses compared to smaller tanks due the resulting lower flow velocity. However, it should be noted that within the range of realistic tank dimensions, the pressure will neither increase nor decrease by a factor of two.

Numerical simulations using a simplified 1D-2P were conducted to visualize the temperature distribution within the tank. This simplified simulations provide valuable insights into how specific parameters affect temperature behaviour. Selecting materials with lower diffusivity is advisable when the goal of the system is to maintain a well-defined separation between the hot and cold layers. This is particularly valuable when storing heat in a partially charged tank, resulting in a clear thermocline and efficient separation. Higher mass flows lead to faster charging of the system. In systems with relatively high heat transfer coefficients, the fluid and solid temperatures closely align, allowing for an equivalent temperature approximation.

Future investigations could involve conducting experiments to assess the feasibility of pumping air through the packed bed at high velocities. Furthermore, it is crucial to ascertain whether the solid particles can absorb all the heat transported through the system, ensuring that the temperature of the exiting heat flow equals the lower temperature limit and no heat is wasted. Moreover, future research should focus on investigating the influence of tank shape on the resulting flow conditions. Lastly, it is necessary to elaborate the existing numerical model to enable the simulation of the real-scale system, as this aspect was not realized in the current study.

Appendix A. Steel Industry Waste Heat

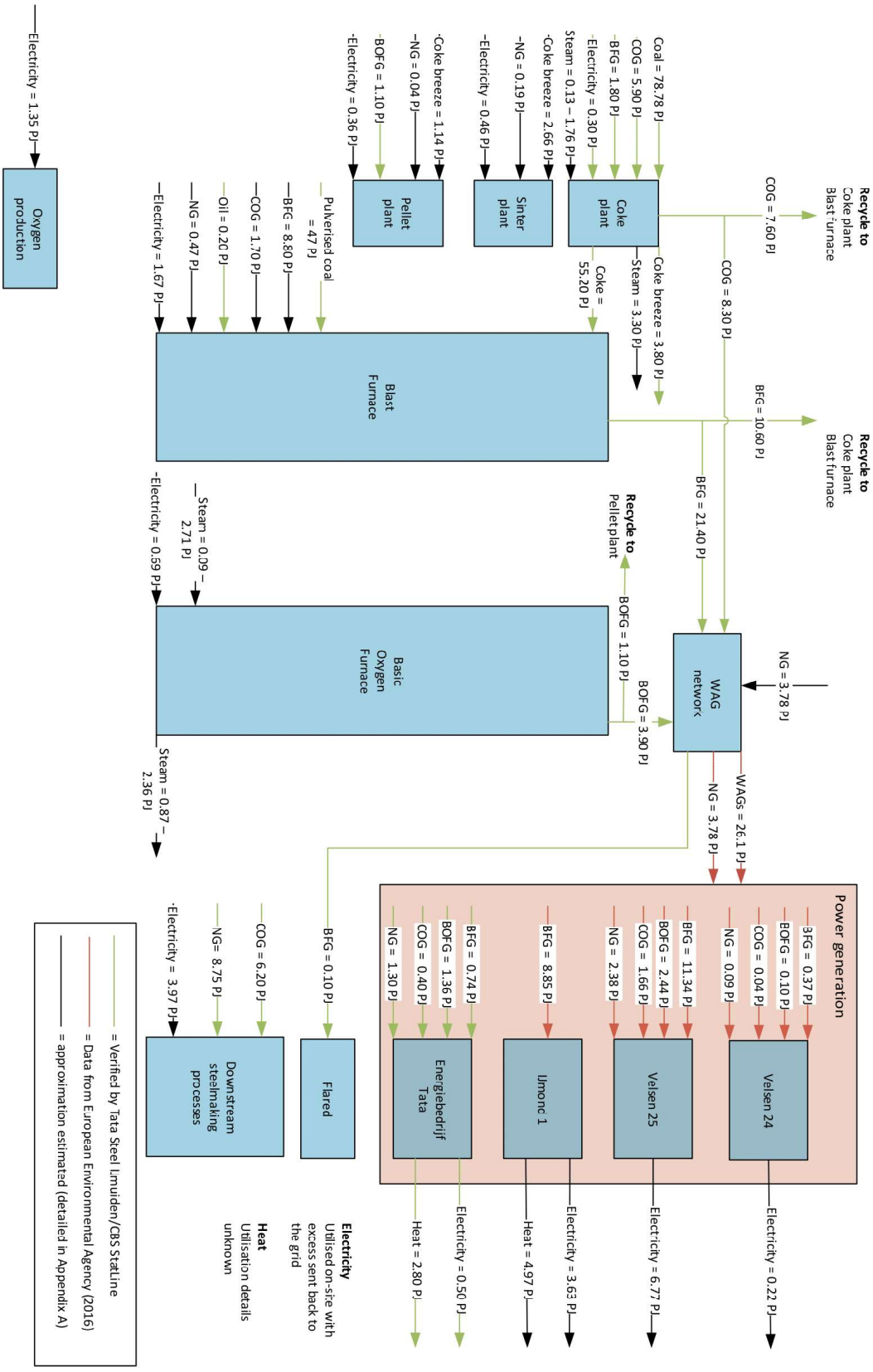

Figure A.17: Overview of the annual energy flow at TATA steel in 2017 (Daniels et al., 2019).

Appendix B. Models and Assumptions

Appendix B.1. Existing Numerical Models

The effective volumetric heat capacity is found by summing the contributions to the volumetric heat capacity by the fluid and solid phase. The weight of its contribution is determined by the porosity of the packed bed.

$$(\rho c_p)_{eff} = \epsilon(\rho c_p)_f + (1-\epsilon)(\rho c_p)_s \tag{B.1}$$

The same principle holds for the effective conductivity

$$k_{eff} = \epsilon k_f + (1-\epsilon)k_s \tag{B.2}$$

Which can be split in:

$$k_{f,eff} = \epsilon k_f \tag{B.3}$$

$$k_{s,eff} = (1-\epsilon)k_s \tag{B.4}$$

The velocity of the HTF is determined by dividing the desired mass flow rate by the product of the fluid phase density and the combined factors of porosity and cross-sectional area of the packed bed.

$$v = \frac{\dot{m}}{\rho_f \left(\epsilon\pi\left(\frac{D}{2}\right)^2\right)} \tag{B.5}$$

Appendix B.2. Model Results Comparison

In addition to the presented Solar One project, two other primary examples of PBTS experiments are the Promes-CNRS Laboratory demonstrator and the Sandia National Laboratory pilot. The main characteristics of these experiments can be found in Table B.7.

Table B.7: Experiment details and characteristics of the Promes-CNRS Laboratory demonstrator and the Sandia National Laboratory pilot (Hoffmann et al., 2016).

Parameter	Promes-CNRS Laboratory demonstrator	Sandia Laboratory pilot
Capacity	29.9 MJ	8.3 GJ
HTF	Rapeseed oil	Solar salt
Storage Material	Quartzite rock	Quartzite rock and sand
Discharge time	3 h	3 h
Tank height	1.8 m	6.1 m
Tank Diameter	0.4 m	3 m m
Volume	0.25 m^3	42 m^3
Porosity	0.41	0.22
Particle Diameter	4.0 cm	1.91 cm
HTF Mass flow rate	0.019 kg/s	5.46 kg/s
T_{hot}	210°C	395.9°C
T_{cold}	160°C	289°C

The resulting from these two experiments can be seen in Figure B.18 and Figure B.19 for the Promes-CNRS Laboratory demonstrator and the Sandia National Laboratory pilot respectively. One key finding from these results is that as the PBTS system decreases in size, the discrepancy between the predicted and actual temperature increases. The average mean error for the Promes-CNRS Laboratory demonstrator (the smallest storage tank setup) is reported as 1.75°C and 1.32°C and the maximum error as 7.7°C and 6.4°C for the 1D-1P and 1D-2P models respectively. Note that the errors observed in the larger Sandia Laboratory pilot system are already significantly smaller compared to those observed in the smaller-scale system.

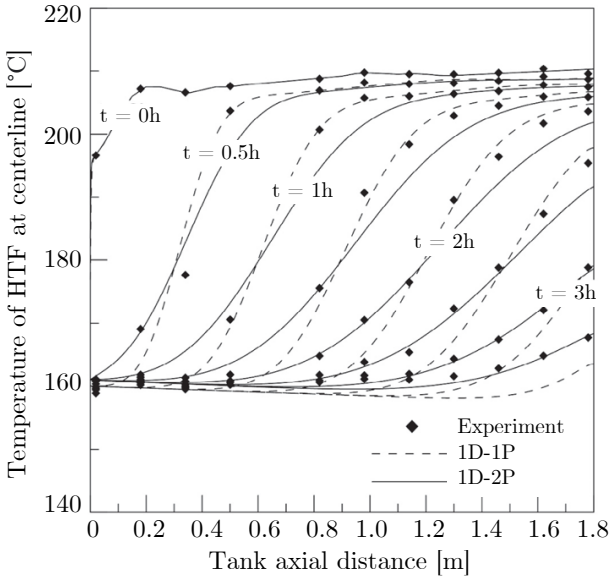

Figure B.18: Comparison of data from the single and two phase (CS) model compared to experimental data from the Promes-CNRS Laboratory demonstrator (Hoffmann et al., 2016).

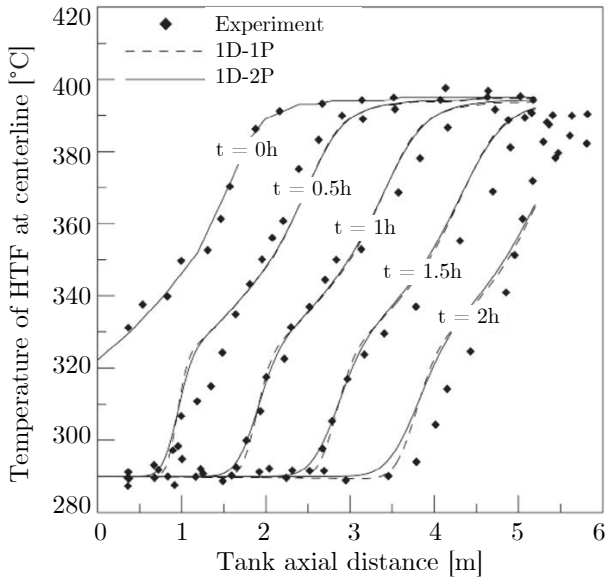

Figure B.19: Comparison of data from the single and two phase (CS) model compared to experimental data from the Sandia Laboratory pilot (Hoffmann et al., 2016).

Appendix C. Classifications

Appendix C.1. Characteristic Biot Length Scale Derivation

When considering a particle with a Biot number typically below 0.1, the lumped capacitance method can be applied. It is then presumed that the particle maintains a uniform temperature throughout its volume. In such cases, Newton's cooling law can be employed to characterize the cooling process of a solid body in a convective environment. The law can be expressed as follows:

$$mc_p \frac{dT}{dt} = hA(T - T_{sur}) \tag{C.1}$$

Where the mass of the body is defined as:

$$m = \rho V \tag{C.2}$$

Both side are integrated over time:

$$\int_{T(t)}^{T_i} \frac{dT}{T_{sur}} dt = \int \frac{hA}{\rho V c_p} dt \tag{C.3}$$

$$ln\left(\frac{T(s) - T_{sur}}{T_i - T_{sur}}\right) = \frac{hA}{\rho V c_p} t \tag{C.4}$$

This expression is then re-written as:

$$\frac{T(s) - T_{sur}}{T_i - T_{sur}} = e^{\frac{hA}{\rho V c_p} t} \tag{C.5}$$

$$T(t) = (T_0 - T_{sur}) e^{-\frac{hA}{\rho c_p V} t} + T_{sur} \tag{C.6}$$

Note how the exponential of the first term on the right side is re-defined as:

$$T(t) = (T_i - T_{sur}) e^{-BiFo} + T_{sur} \tag{C.7}$$

Where:

$$Bi = \frac{hL_c}{k} \tag{C.8}$$

And it thus follows that the characteristic length is:

$$L_c = \frac{V}{A} \tag{C.9}$$

For a sphere is holds that:

$$L_{c,sphere} = \frac{d}{6} \tag{C.10}$$

Appendix C.2. Biot Table

To determine the dimensionless temperature at a particular point within a spherical particle, it is necessary to ascertain the values of the constants A_1 and λ_1, which are utilized in Equation 19. The values of the constants A_1 and λ_1 can be acquired by calculating the Biot number and referring to the table below for their corresponding values:

Table C.8: The numerical values of the constants A_1 and λ_1 are provided as a function of the Biot number specifically for spherical particles (Cengel et al., 2008).

Biot	λ_1	A_1
0.01	0.1730	1.0030
0.02	0.2445	1.0060
0.04	0.3450	1.0120
0.06	0.4217	1.0179
0.08	0.4860	1.0239
0.1	0.5423	1.0298
0.2	0.7593	1.0592
0.3	0.9208	1.0880
0.4	1.0528	1.1164
0.5	1.1656	1.1441
0.6	1.2644	1.1713
0.7	1.3525	1.1978
0.8	1.4320	1.2236
0.9	1.5044	1.2488
1.0	1.5708	1.2732
2.0	2.0288	1.4793
3.0	2.2889	1.6227
4.0	2.4556	1.7202
5.0	2.5704	1.7870
6.0	2.6537	1.8338
7.0	2.7165	1.8673
8.0	2.7654	1.8920
9.0	2.8044	1.9106
10.0	2.8363	1.9249
20.0	2.9857	1.9781
30.0	3.0372	1.9898
40.0	3.0632	1.9942
50.0	3.0788	1.9962
100.0	3.1102	1.9990

Appendix C.3. Heisler Analysis Validation

To verify the accuracy of the method employed to create Figure 13, a reconstruction of a graph presented in reliable literature was made. Figure C.20, sourced from the book 'Fundamentals of Heat and Mass Transfer' authored by Incropera et al. (2006), served as the basis for comparison. Additionally, Figure C.21 was generated using the method outlined in Section 5.4. As can be seen the two graphs show almost identical values, thus indicating the validity of the utilized method and the reliability of the obtained results.

Appendix C.4. Heat Equation

The heat equation presented allows for analytical solutions to one-dimensional heat transfer problems. By specifying boundary conditions, the temperature distribution within an object can be determined. However, due to the scope of this study, analytical solutions to these temperature distributions are not worked-out. Instead, simplified approximations are employed to estimate the temperature distribution.

$$\frac{\partial T}{\partial t} = k \frac{\partial^2 T}{\partial x^2} \tag{C.11}$$

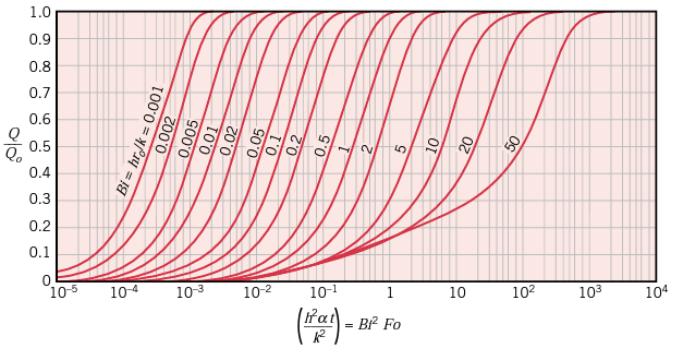

Figure C.20: Heisler chart presented in literature: 'Internal energy change as a function of time for a sphere of radius r_0' (Incropera et al., 2006).

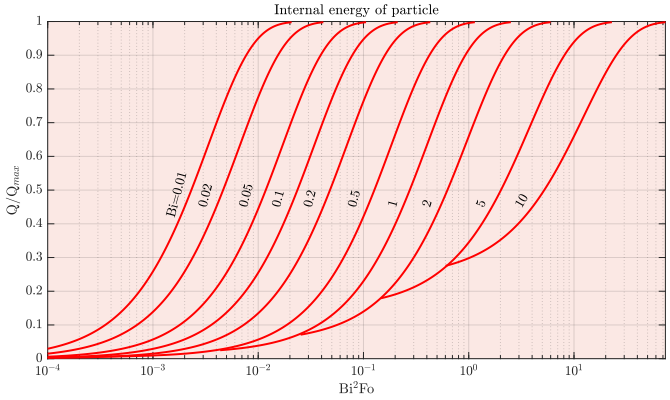

Figure C.21: Reproduction of Heisler chart for spherical particle corresponding to the one presented in the book 'Fundamentals of Heat and Mass Transfer'.

Appendix D. Thermocline Model

Figure D.22 presents results of the same model as depicted in Figure 16. The difference is that the source term, which governs the amount of heat transfer between the solid and the fluid phase, is set to five instead of one. The result is that the temperature profiles of both phases lie closer together.

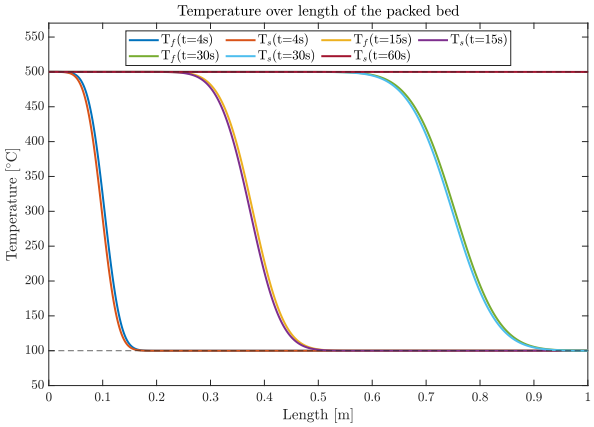

Figure D.22: Resulting fluid and solid temperature profiles from the continous solid phase model. The source term set to a value of five for both the fluid and solid phase. The enhanced heat transfer means the temperatures of the solid and fluid components exhibit a reduced separation.

Figure D.23 shows the result of a simulation with increased diffusivity for both the fluid and solid phase. The diffusivity in this simulation is set to 1e-3 m^2/s instead of the previous 1e-5 m^2/s. The result is that the thermocline is less steep indicating the separation between the cold and hot layer is less effective.

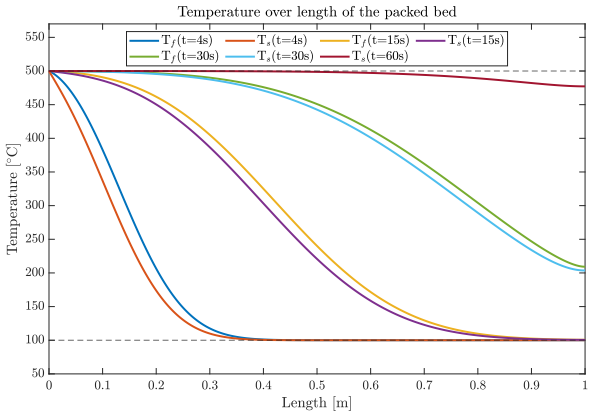

Figure D.23: Resulting fluid and solid temperature profiles from the continous solid phase model. The diffusivity set to a value of 1e-3 for both the fluid and solid phase. The higher diffusivity leads to a broader dispersion of temperature throughout the tank, resulting in a less pronounced thermocline. As a consequence, the reduced steepness of the thermocline signifies a decrease in the efficiency of heat separation.

Figure D.24 shows the result of a simulation with increased fluid velocity. The velocity in this simulation is set to 0.1 m/s instead of the previous 0.05 m/s. This results in faster (dis)charge times of the PTSB system.

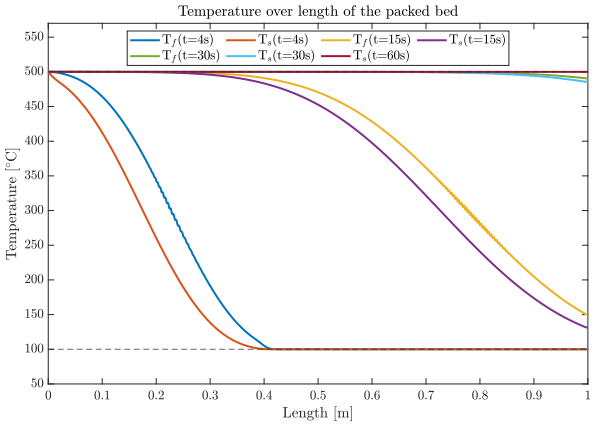

Figure D.24: Resulting fluid and solid temperature profiles from the continous solid phase model. The flow velocity is set to 0.1 m/s. The higher velocity means more heat enters the system and the system is charged quicker.

References

Alami, K.E., Asbik, M., Zari, N., Rachidi, S., 2018. Thermocline thermal storage using a packed bed of moroccan rocks. IOP Conference Series: Earth and Environmental Science 161, 012016. doi:10.1088/1755-1315/161/1/012016.

Avallone, F., 2018. Modeling of a thermocline thermal energy storage: application to a concentrating solar power plant .

Bejan, A., 1993. Heat Transfer. Wiley. URL: https://books.google.nl/books?id=TgtRAAAAMAAJ.

Benyahia, F., O'Neill, K.E., 2005. Enhanced voidage correlations for packed beds of various particle shapes and sizes. Particulate Science and Technology 23. doi:10.1080/02726350590922242.

Cengel, Y.A., Turner, R.H., Cimbala, J.M., 2008. Fundamentals of Thermal-Fluid Sciences. McGraw-Hill Education. doi:10.1115/1.802600.

Chekifi, T., Boukraa, M., 2023. Cfd applications for sensible heat storage: A comprehensive review of numerical studies. Journal of Energy Storage 68, 107893. doi:10.1016/j.est.2023.107893.

Cui, Z., Chen, H., He, Y., Yang, Y., 2012. Effects of heat transfer on pressure drop in laminar flow microchannels. Journal of Heat Transfer 134, 031023. doi:10.1115/1.4005098.

Daniels, B., van Hout, M., Keys, A., 2019. Decarbonisation options for the dutch steel industry.

Ergun, S., 1952. Fluid flow through packed columns. Chemical Engineering Progress 48, 89–94.

van Esch, B., 2018. Thermal and Fluid Engineering. Eindhoven University of Technology.

Eurostat, 2020. Energy, transport and environment statistics : 2020 edition. Publications Office. doi:doi/10.2785/522192.

Fei, W., Narsilio, G.A., Disfani, M.M., 2019. Impact of three-dimensional sphericity and roundness on heat transfer in granular materials. Powder Technology 355, 770–781. doi:10.1016/j.powtec.2019.07.094.

Fletcher, W.D., Smith, C.B., 2020. International efforts to address global warming. doi:10.1016/B978-0-12-823366-5.00008-7.

Galione, P., Pérez-Segarra, C., Rodríguez, I., Torras, S., Rigola, J., 2015. Numerical evaluation of multi-layered solid-pcm thermocline-like tanks as thermal energy storage systems for csp applications. Energy Procedia 69, 832–841. doi:10.1016/j.egypro.2015.03.099.

Gamesa, S., 2022. 2nd life for power plants using electric thermal energy storage (etes).

Handley, D., Heggs, P., 1969. The effect of thermal conductivity of the packing material on transient heat transfer in a fixed bed. International Journal of Heat and Mass Transfer 12, 549–570. doi:10.1016/0017-9310(69)90038-6.

Hoffmann, J.F., Fasquelle, T., Goetz, V., Py, X., 2016. A thermocline thermal energy storage system with filler materials for concentrated solar power plants: Experimental data and numerical model sensitivity to different experimental tank scales. Applied Thermal Engineering 100, 753–761. doi:https://doi.org/10.1016/j.applthermaleng.2016.01.110.

IEA, 2021. Key world energy statistics 2021.

Imai, T., Murayama, T., Ono, Y., 1994. The effect of structure of packed beds on the convective heat transfer coefficient between particle and liquid. ISIJ International 34, 777–783. doi:10.2355/isijinternational.34.777.

Incropera, F., de Witt, F., Bergman, T., Lavine, A., 2006. Fundamentals of Heat and Mass Transfer. 6th ed., John Wiley Sons, Inc.

Ismail, K., Stuginsky Jr, R., 1999. A parametric study on possible fixed bed models for pcm and sensible heat storage. Applied Thermal Engineering 19, 757–788. doi:10.1016/S1359-4311(98)00081-7.

Knobloch, K., Ulrich, T., Bahl, C., Engelbrecht, K., 2022. Degradation of a rock bed thermal energy storage system. Applied Thermal Engineering 214, 118823. doi:10.1016/j.applthermaleng.2022.118823.

Mao, A., Park, J.H., Han, G.Y., Seo, T., Kang, Y., 2010. Heat transfer characteristics of high temperature molten salt for storage of thermal energy. Korean Journal of Chemical Engineering 27, 1452–1457. doi:10.1007/s11814-010-0260-1.

Miranda, M., Matos, C., Rodrigues, N., et al., 2019. Effect of temperature on the thermal conductivity of a granite with high heat production from central portugal. Journal of Iberian Geology 45, 147–161. doi:10.1007/s41513-018-0096-9.

Niedermeier, K., Marocco, L., Flesch, J., Mohan, G., Coventry, J., Wetzel, T., 2018. Performance of molten sodium vs. molten salts in a packed bed thermal energy storage. Applied Thermal Engineering 141, 368–377. doi:10.1016/j.applthermaleng.2018.05.080.

Odenthal, C., Klasing, F., Bauer, T., 2019. A three-equation thermocline thermal energy storage model for bidisperse packed beds. Solar Energy 191, 410–419. doi:10.1016/j.solener.2019.09.005.

Ortega-Fernández, I., Rodríguez-Aseguinolaza, J., 2019. Thermal energy storage for waste heat recovery in the steelworks: The case study of the reslag project. Applied Energy 237, 708–719. doi:10.1016/j.apenergy.2019.01.007.

Papapetrou, M., Kosmadakis, G., Cipollina, A., La Commare, U., Micale, G., 2018. Industrial waste heat: Estimation of the technically available resource in the eu per industrial sector, temperature level and country. Applied Thermal Engineering 138, 207–216. doi:https://doi.org/10.1016/j.applthermaleng.2018.04.043.

Robertson, E.C., 1988. Thermal properties of rocks.

Schumann, T., 1929. Heat transfer: A liquid flowing through a porous prism. Journal of the Franklin Institute 208, 405–416. doi:10.1016/S0016-0032(29)91186-8.

Seyitini, L., Belgasim, B., Enweremadu, C.C., 2023. Solid state sensible heat storage technology for industrial applications – a review. Journal of Energy Storage 62, 106919. doi:10.1016/J.EST.2023.106919.

Singh, R., Saini, R., Saini, J., 2006. Nusselt number and friction factor correlations for packed bed solar energy storage system having large sized elements of different shapes. Solar Energy 80, 760–771. doi:10.1016/j.solener.2005.07.001.

Strasser, M.N., Selvam, R.P., 2012. A cost and performance comparison of packed bed and structured thermocline thermal energy storage systems doi:https://doi.org/10.1016/j.solener.2014.07.023.

Tanaka, N., 1979. Waste heat recovery from sintering plants. Tetsu-to-Hagani 20.

Ulusoy, U., 2019. Quantifying of particle shape differences of differently milled barite using a novel technique: Dynamic image analysis. Materialia 8, 100434. doi:10.1016/j.mtla.2019.100434.

Wakao, N., Kaguei, S., Funazkri, T., 1979. Effect of fluid dispersion coefficients on particle-to-fluid heat transfer coefficients in packed beds: Correlation of nusselt numbers. Chemical Engineering Science 34, 325–336. doi:10.1016/0009-2509(79)85064-2.

Whitaker, S., 1972. Forced convection heat transfer correlations for flow in pipes, past flat plates, single cylinders, single spheres, and for flow in packed beds and tube bundles. AIChE Journal 18, 361 – 371. doi:10.1002/aic.690180219.

Yang, X., Yang, X., Ding, J., Shao, Y., Qin, F.G., Jiang, R., 2012. Criteria for performance improvement of a molten salt thermocline storage system. Applied Thermal Engineering 48, 24–31. doi:10.1016/j.applthermaleng.2012.04.046.

Yunus Cengel, Y.A., Cimbala, J.M., Turner, R.H., 2018. Fundamentals of Thermal-Fluid Sciences. Springer. doi:10.1007/978-3-662-52989-8.

Zhang, S., Zhao, L., Feng, J., Luo, X., Dong, H., 2019. Thermal analysis of sinter vertical cooler based on waste heat recovery. Applied Thermal Engineering 157. doi:10.1016/J.APPLTHERMALENG.2019.04.118.